Journal of Power Electronics (2022) 22:50–60
https://doi.org/10.1007/s43236-021-00340-7

ORIGINAL ARTICLE

Initial rotor position and inductance estimation of PMSMs utilizing zero-current-clamping effect

Jing Wang[1] · Jianhu Yan[1] · Zhanfeng Ying[2]

Received: 29 June 2021 / Revised: 27 October 2021 / Accepted: 28 October 2021 / Published online: 10 November 2021

Abstract
The high-frequency (HF) signal injection method can be used for estimating the initial rotor position and the *d-q* axis inductances of a permanent magnet synchronous machine (PMSM). Low amplitude signal injection is beneficial to keep the rotor stationary and to reduce HF noise. However, it seriously suffers from dead-time. In this paper, the influence of dead-time on the injected signal is analyzed, and a method for estimating the initial rotor position and *d-q* axis inductances of a PMSM is proposed by utilizing the zero-current-clamping (ZCC) effect. Signal injection is carried out in the three-phase stationary reference frame. Therefore, the analysis of the dead-time effect can be simplified, and the initial rotor position and the *d-q* axis inductances can be simultaneously estimated. First, the ZCC effect is analyzed in detail when two-phase power switches operate at the same duty ratio. A linear relationship is then built between the injected HF voltage and the current variation. Based on this, the algorithms of the parameter estimations are derived. Moreover, to improve the estimation accuracy, the least square method is used to reduce the influence of the measured errors caused by current sensors. Finally, a PMSM driven experimental system is built and tested to verify the proposed method.

Keywords Dead-time · High-frequency voltage signal injection · Inductance estimation · Initial rotor position estimation · Zero-current-clamping

1 Introduction

A permanent magnet synchronous machine (PMSM) has the advantages of a high efficiency and a high power density, which is suitable for many industrial applications [1, 2]. To achieve a reliable startup of a PMSM with the sensorless control method, the main motor parameters should be obtained including the initial rotor position, the *d-q* axis inductances, and the winding resistances. The initial rotor position is used for field-oriented control. The parameter design of the controller and observer can be realized according to the inductances and resistances. High-frequency (HF) voltage signal injection is the conventional method for estimating the rotor position and *d-q* axis inductances at standstill, including the HF rotating signal injection method and the HF pulsating signal injection method [3–5].

The rotor position can be obtained from measured HF signals utilizing the mechanical or magnetic saturation saliencies. To solve the defects of conventional methods such as complicated signal demodulation and HF noise, many improved methods have been proposed in the past decade. In [6], a discrete Fourier transform is adopted for detecting the rotor sector so the time of initial position estimation is only half of an injection cycle. In [7], a conventional band-pass filter is substituted for an all-pass filter to eliminate the phase lag of the HF signal demodulation process. In [8], a pseudorandom HF square wave voltage was used for suppressing HF noise.

Keeping the rotor stationary is critical for initial rotor position estimation. Thus, the injected HF signal should have a low amplitude to mitigate the additional torque caused by the injected signal. However, inverter nonlinearity, especially dead-time and ZCC effects, can result in additional current harmonics, output voltage vector variations, and distortion of the injected signal [9–11]. At low and zero speeds, inverter nonlinearity has a severe influence on parameter

✉ Jianhu Yan
yanjianhu@njust.edu.cn

1 School of Automation, Nanjing University of Science and Technology, Nanjing, China

2 School of Energy and Power Engineering, Nanjing University of Science and Technology, Nanjing, China

estimations [12]. In [13], the inverter nonlinearity effects on HF signal injection were investigated, and voltage error and harmonic current are described. In [14], adaptive linear neurons were adopted for estimating and suppressing current harmonics with inverter nonlinearity. In [15], a vectorial disturbance estimator was proposed to estimate and compensate the voltage vector variation. In [16], voltages in a trapezoidal form were utilized to compensate for inverter nonlinearity.

Although many conventional HF signal injection methods have been used for estimating rotor position and inductances, their analyses of dead-time effect are insufficient, especially the ZCC effect. In the conventional methods, the output voltage variation caused by dead-time is considered to be a constant, which is incorrect under low amplitude HF excitation. In this paper, a method for simultaneously estimating initial rotor position and inductances was proposed based on HF pulsating voltage signal injection using the ZCC effect under the condition of low-amplitude HF excitation and a severe dead-time.

The remainder of this paper is organized as follows. Dead-time and ZCC effects are both analyzed in detail in Sect. 2. A method for initial rotor position and *d*-*q* axis inductance estimations is derived in Sect. 3. In Sect. 4, a PMSM driven experimental system is built and tested to verify the proposed method. Although many advanced algorithms have been proposed for parameter estimations or for reducing dead-time effect, the method proposed in this paper can avoid complex signal demodulation and observer design processes. In addition, it can obtain the initial rotor position and inductances easily.

2 Dead-time effect analysis

2.1 Asymmetric currents caused by dead-time

Figure 1 shows a diagram of a three-phase voltage source inverter (VSI) with PMSM. U_{dc} is the DC bus voltage. S_a^+, S_a^-, S_b^+, S_b^-, S_c^+, and S_c^- are the *A*, *B*, and *C* phase upper and lower arm driving signals of the power switches, respectively. The phase current direction shown in Fig. 1 denotes that the current polarity is positive. According to the space vector pulse width modulation (SVPWM), the non-zero basic space voltage vectors and the corresponding switching states (S_a^+, S_b^+, S_c^+) are shown in Fig. 2. The amplitudes of these basic space voltage vectors are the same, $2U_{dc}/3$, except for the zero vectors '000' and '111'.

The inverter switching period is recorded as T_s. Meanwhile, the three-phase currents are sampled at the beginning of each switching period. The injected voltage signal is a pulsating square wave signal, where the amplitude and period are set as U_o and $4T_s$, respectively. According to the SVPWM, the resultant output voltage vectors consist of U_3, U_4 and zero vectors when the direction of the HF voltage signal injection is '*a*', as shown in Fig. 2. Furthermore, the power switches of the *B* and *C* phases operate at the same duty ratio. If two-phase power switches operate at the same duty ratio, the same HF voltage signals are injected. Moreover, the resistive voltage drop can be neglected in comparison with the inductive voltage drop under HF signal excitation. Therefore, their currents have the same frequencies and phases and cross the zero level simultaneously in the steady state. For the Y-connected windings of the PMSM, if the two-phase currents are zero, the third phase current is also zero. Therefore, the three-phase currents simultaneously cross the zero level, which is essential for the analysis of the dead-time effect. Figure 3 shows simulations of the reference voltage and the corresponding steady-state three-phase currents (T_s is 0.1 ms). The reference voltage is given in Fig. 3a and it produces symmetric steady-state currents as shown in Fig. 3b without dead-time. In practice, dead-time can distort actual voltage and cause asymmetric steady-state currents, as shown in Fig. 3c.

2.2 Dead-time effect analysis with different HF voltage amplitudes

The phase *A* current is taken as an example to analyze the dead-time effect on an injected signal. Its waveform in an

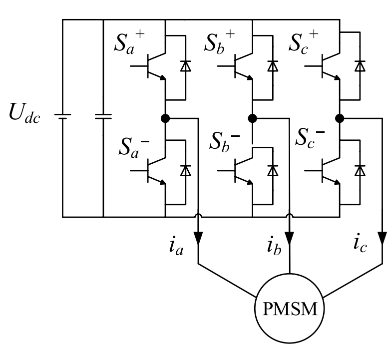

Fig. 1 Three-phase voltage source inverter

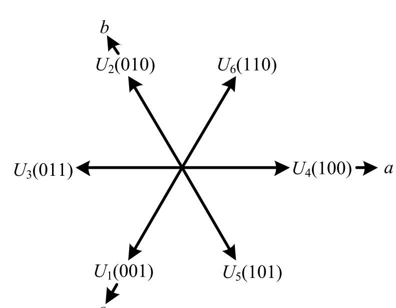

Fig. 2 Basic voltage vectors based on SVPWM

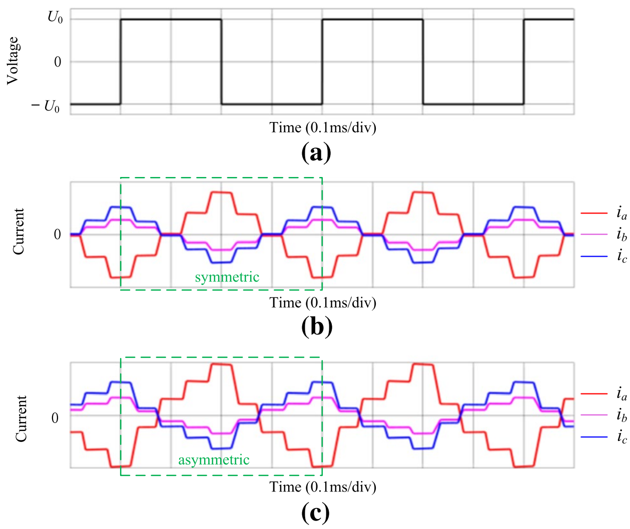

Fig. 3 Reference voltage and corresponding steady-state three-phase currents under a 10 kHz switching frequency: **a** reference voltage; **b** three-phase currents without dead-time; **c** three-phase currents with dead-time

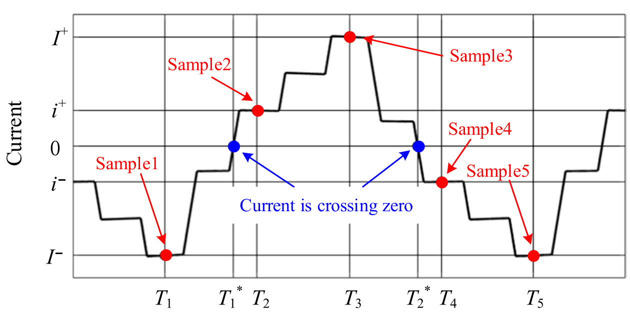

Fig. 4 Phase *A* current in an injected signal period

injected signal period is detailed in Fig. 4, where T_1-T_5 is one injected signal period including four switching periods: T_1-T_2, T_2-T_3, T_3-T_4, and T_4-T_5. It can be seen that the phase *A* current crosses the zero level at T_1^* and T_2^*. I^-, i^-, i^+, and I^+ are the sampling values of the phase *A* current at T_1, T_2, T_3, and T_4, respectively.

During T_1-T_2 or T_2-T_3, the reference voltage amplitude is U_o. T_a, T_b, and T_c are the conducting times of the power switches of the *A*, *B*, and *C* phase upper arms, respectively. T_a, and T_b can be expressed according to SVPWM algorithm as:

$$\begin{cases} T_a = \dfrac{1}{2}(1 + \dfrac{3U_o}{2U_{dc}})T_s \\ T_b = T_c = \dfrac{1}{2}(1 - \dfrac{3U_o}{2U_{dc}})T_s \end{cases} \tag{1}$$

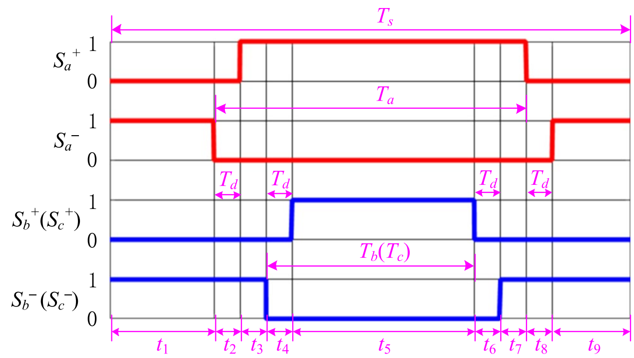

Fig. 5 Nine switching states in a switching period

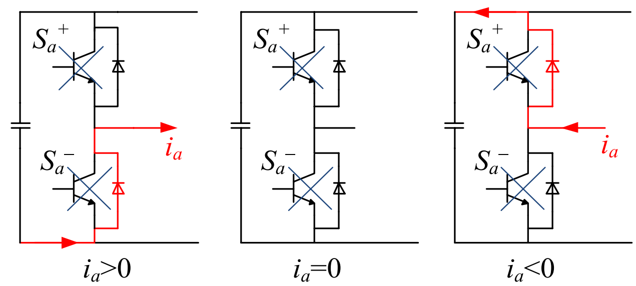

Fig. 6 Phase *A* current during dead-time

According to the different switching states of the inverter, every switching period can be divided into nine intervals noted as t_k ($k = 1, 2, \ldots, 9$), as shown in Fig. 5.

The dead-time effect on the reference voltage is mainly related to the three-phase current polarities. Since the power switches of phases *B* and *C* operate at the same duty ratio, the three-phase current polarities have three possible states: (a) $i_a > 0$, $i_b < 0$, $i_c < 0$; (b) $i_a < 0$, $i_b > 0$, $i_c > 0$; and (c) $i_a = i_b = i_c = 0$. Figure 6 shows the phase *A* current during the dead-time. The lower arm can be considered to turn on when $i_a > 0$, and the upper arm can be considered to turn on when $i_a < 0$. If the phase *A* current crosses the zero level during the dead time, it clamps to zero and remain at the zero level until the switching states change, which is the ZCC effect. The phase *B* and *C* currents are similar to the phase *A* current. In regard to the different current polarities and switching states, the basic voltage vector corresponding to each interval t_k is recorded as u_k. Table 1 lists t_k and u_k, where '0' denotes the zero vector and T_d denotes the dead-time. The basic voltage vector is derived from Fig. 5. For example, at t_3, $S_a^+ = 1$, $S_b^+ = 0$, and $S_c^+ = 0$. Thus, the voltage vector is U_4 (100). In the dead-time, according to Fig. 6, $S_a^+ = 0(i_a > 0$ or $i_a = 0)$, $S_a^+ = 1(i_a < 0)$. The phase *B* and phase *C* currents are similar to those of phase *A*.

It can be found from Table 1 that the resultant voltage vector still consists of U_4 and zero vectors even though the dead-time has already led to a distortion. It states that the

Table 1 Output basic voltage vectors in a switching period

t_k	Time	$i_a>0$	$i_a=0$	$i_a<0$
t_1	$(T_s-T_a-T_d)/2$	0	0	0
t_2	T_d	0	0	U_4
t_3	$(T_a-T_b)/2-T_d$	U_4	U_4	U_4
t_4	T_d	0	0	U_4
t_5	T_b-T_d	0	0	0
t_6	T_d	0	0	U_4
t_7	$(T_a-T_b)/2-T_d$	U_4	U_4	U_4
t_8	T_d	0	0	U_4
t_9	$(T_s-T_a-T_d)/2$	0	0	0

dead-time is unable to change the voltage vector direction in this case. Consequently, U_4 can be substituted by its amplitude $2U_{dc}/3$ to calculate the resultant voltage vector. During T_2-T_3, the phase A current polarity is positive. According to Table 1, the resultant voltage amplitude U_{avg} in a switching period can be expressed as:

$$U_{avg} = \sum_{k=1}^{9} \frac{t_k}{T_s} u_k = \frac{T_a - T_b - 2T_d}{T_s} \cdot \frac{2}{3} U_{dc} \tag{2}$$

By submitting (1) into (2), the distorted voltage drop U_{err} can be obtained as:

$$U_{err} = U_o - U_{avg} = \frac{T_d}{T_s} \cdot \frac{4}{3} U_{dc} \tag{3}$$

This indicates that U_{err} is actually independent of U_o. During the time period T_1-T_2, the polarities of the three-phase currents are changed. From Fig. 4, under the assumption that the variations of inductance and resistance are neglected, I^- ($i_a<0$) and I^+ ($i_a>0$) can be expressed as:

$$\begin{cases} -L_a \frac{I^-}{T_s} = \sum\limits_{k=1}^{j-1} \frac{t_k}{T_s} u_k + \frac{t_j - t_x}{T_s} u_j \\ L_a \frac{I^+}{T_s} = U_o - U_{err} + \sum\limits_{k=j+1}^{9} \frac{t_k}{T_s} u_k + \frac{t_x}{T_s} u_j \\ 0 < t_x < t_j \end{cases} \tag{4}$$

where t_j ($j=2, 3, 4, 6, 7$) is one of nine intervals shown in Fig. 5. During this interval, the phase A current crosses the zero level. In addition, $i_a<0$ during t_j–t_x, and $i_a=0$ or $i_a>0$ during t_x. L_a is the phase A inductance, which is a constant value at standstill. Since the average value of the HF voltage signal is zero in each injected signal cycle, the relationship between I^- and I^+ can be described as:

$$I^+ + I^- = 0 \tag{5}$$

In addition, i^+ in Fig. 4 can be expressed as:

Table 2 Relationship between U_o and i^+

t_j	$r=U_o/U_{err}$	$L_a i^+/T_s$
t_2	$1<r<1.25$	U_o-U_{err}
t_3	$1.25<r<1.5$	$0.25U_{err}$
t_4 or t_6	$1.5<r<2.5$	$(U_o-U_{err})/2$
t_7	$2.5<r$	$0.75U_{err}$

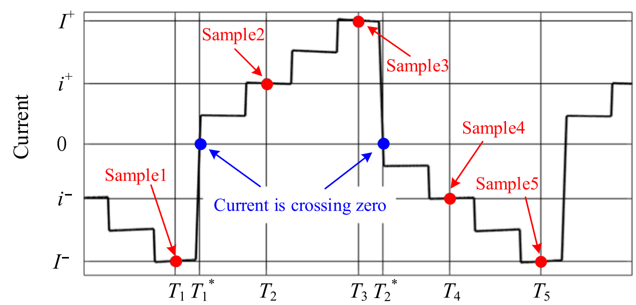

Fig. 7 Phase A current when $1.25<r<1.5$

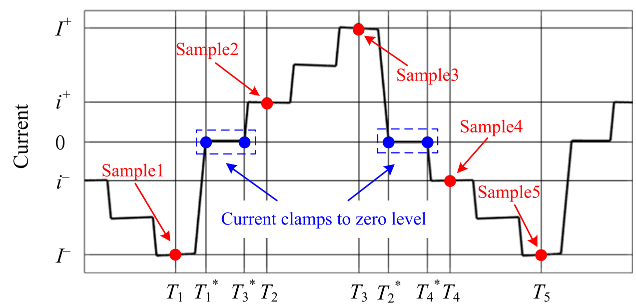

Fig. 8 Phase A current when $1.5<r<2.5$

$$L_a \frac{i^+}{T_s} = \sum_{k=j+1}^{9} \frac{t_k}{T_s} u_k + \frac{t_x}{T_s} u_j \tag{6}$$

According to (4–6), U_o and i^+ can be derived corresponding to different values of j and shown in Table 2.where r is defined as U_o/U_{err} for the sake of simplicity. Due to symmetry, the analytical methods and results during T_3-T_5 are similar to those during T_1-T_3.

In fact, the phase A current shown in Fig. 4 corresponds to $r>2.5$. Figure 7 shows the phase A current when $1.25<r<1.5$. In Fig. 4 and Fig. 7, both of the currents do not clamp to the zero level. Figure 8 shows the phase A current when $1.5<r<2.5$. It is evident that the phase A current clamps to zero during $T_1^*-T_3^*$ and $T_2^*-T_4^*$. This operating state is used for realizing the parameter estimation.

Obviously, dead-time is a main factor that leads to inverter nonlinearity. In addition, the threshold voltages of the active switch, the freewheeling diode, and the turn-on and turn-off time delays of the switch incur signal distortions. The variation of the output voltage amplitude caused by inverter nonlinearity can be measured more accurately through a simple experiment. The inverter generates a constant voltage vector that is equal to the DC voltage, which has the same direction along with U_4. This means that the phase A upper arm turns on, and the phase B and phase C lower arms turn on while the inverter outputs non-zero voltage. An equivalent circuit of this simple experiment is shown in Fig. 9. Here, L_a, L_b, and L_c are the three-phase inductances, R_s is the phase resistance, and i_{avg} is the steady-state average current of phase A.

In the steady-state, the inductive average voltage drop is zero. The relationship between the output voltage U_o and the steady-state phase A average current i_{avg} can be obtained as:

$$U_o = 1.5R_s i_{avg} + U_{err} \tag{7}$$

The least-square method can be adopted for fitting different values of U_o and i_{avg}. The slope of the fitting line is $1.5R_s$ and its intercept is U_{err}.

3 Initial rotor position and inductance estimations

As discussed in Sect. 2, the relationship between the HF voltage amplitude and the dead-time effect as well as a sufficient condition for the ZCC effect are presented, based on which a parameter estimation method is used. The voltage equations of a PMSM at a standstill and the HF excitation in the d-q frame can be expressed as:

$$\begin{cases} u_d = R_h i_d + L_d \dfrac{di_d}{dt} \\ u_q = R_h i_q + L_q \dfrac{di_q}{dt} \end{cases} \tag{8}$$

where u_d and u_q are the d-q axis voltages. i_d and i_q are the d-q axis currents. L_d and L_q are the d-q axis inductances. R_h is the HF resistance. Generally, $L_d \leq L_q$ for a PMSM.

According to (8), the d-axis voltage equation in the time domain can be obtained as:

$$i_{de} = i_{ds}e^{-\lambda} + \frac{u_d}{R_h}(1 - e^{-\lambda}) \tag{9}$$

where i_{ds} and i_{de} are the values of the d-axis current at the beginning and end moments of the d-axis voltage pulse, respectively. λ is $T_h R_h / L_d$ and T_h is the duration during which the currents are not zero. Since HF resistance causes current amplitude attenuation, the HF resistance has less influence on the d-axis current with a shorter T_h. Δi_d denotes the variation of the d-axis current and can be calculated as:

$$\Delta i_d = i_{de} - i_{ds} = \frac{u_d - R_h i_{ds}}{R_h}(1 - e^{-\lambda}) \tag{10}$$

Similarly, Δi_q denotes the variation of the q-axis current and can be calculated as:

$$\Delta i_q = \frac{u_q - R_h i_{qs}}{R_h}(1 - e^{-\eta}) \tag{11}$$

where i_{qs} is the value of the q-axis current at the beginning of a voltage pulse and η is $T_h R_h / L_q$.

As previously mentioned, the range of r should be set to 1.5–2.5 to utilize the ZCC effect, and the phase A current is shown in Fig. 8. Δi_a^+ denotes the variation of the phase A current during $T_3^* - T_2$, where $\Delta i_a^+ = i^+$. From Table 1, the interval corresponding to U_4 is t_7, and the intervals corresponding to the zero vectors are t_8 and t_9. Therefore, T_h can be expressed as:

$$T_h = t_7 + t_8 + t_9 = \frac{1}{2}(T_s - T_b - T_d) \tag{12}$$

By submitting (1) and (3) into (12), T_h can be rewritten as:

$$T_h = \left(\frac{U_o}{2U_{err}} - \frac{1}{2}\right)T_d + \frac{1}{4}T_s = \frac{r-1}{2}T_d + \frac{1}{4}T_s \tag{13}$$

Since the range of r is 1.5–2.5, the maximum value of T_h is 0. $75T_d + 0.25T_s$. Generally, the dead-time T_d is very short. Thus, T_h is also very short and is about a quarter of a

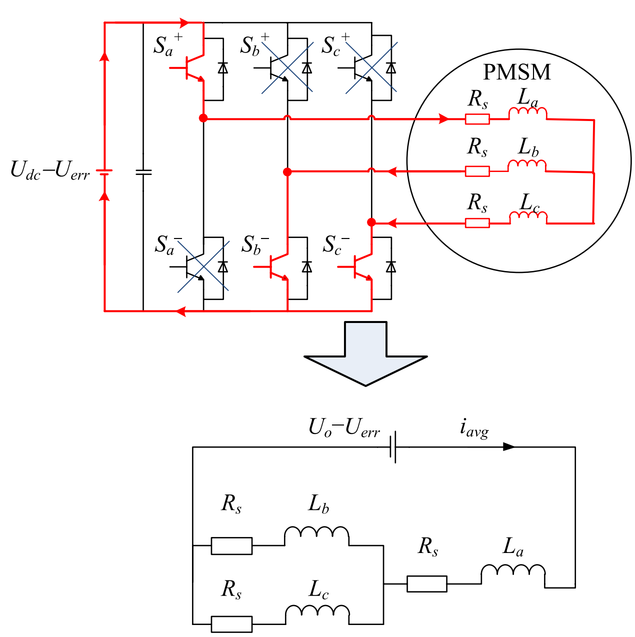

Fig. 9 Equivalent circuit measuring the variation of the output voltage amplitude caused by inverter nonlinearity

switching period. The average output voltage U_h corresponding to T_h can be obtained as:

$$U_h = \frac{t_7}{T_h} \cdot \frac{2}{3} U_{dc} \tag{14}$$

Utilizing the Taylor series for linearization, $e^{-\lambda}$ and $e^{-\eta}$ can be expressed as:

$$\begin{cases} e^{-\lambda} = 1 - \lambda + o(\lambda^2) \approx 1 - \lambda \\ e^{-\eta} = 1 - \eta + o(\eta^2) \approx 1 - \eta \end{cases} \tag{15}$$

where $o(\lambda^2)$ and $o(\eta^2)$ are the second-order errors with respect to the extremely short T_h, which can be neglected. Since the currents clamp to zero during T_1^*–T_3^*, i_{ds} and i_{qs} are equal to zero.

$$i_{ds} = i_{qs} = 0 \tag{16}$$

Since the direction of the HF voltage signal injection is 'a' in the three-phase frame, the equations of the coordinate transformation can be expressed as:

$$\begin{cases} u_d = U_h \cos\theta_a \\ u_q = -U_h \sin\theta_a \\ \Delta i_a^+ = \Delta i_d \cos\theta_a - \Delta i_q \sin\theta_a \end{cases} \tag{17}$$

where θ_a is the electrical angle between the a-axis and the d-axis. According to (10) through (17), Δi_a^+ can be derived as:

$$\frac{\Delta i_a^+}{U_h T_h} = \frac{\cos^2\theta_a}{L_d^+} + \frac{\sin^2\theta_a}{L_q^+} \tag{18}$$

where L_d^+ and L_q^+ are the d-q axis inductances during T_3^*–T_2, which are defined as:

$$\begin{cases} L_d^+ = \frac{\Delta\psi_d}{\Delta i_d} \\ L_q^+ = \frac{\Delta\psi_q}{\Delta i_q} \end{cases} \tag{19}$$

where Δi_d and Δi_q are variations of the d-q axis currents, while $\Delta\psi_d$ and $\Delta\psi_q$ are variations of the d-q axis flux linkages during T_3^*–T_2. It is worth mentioning that R_h is absent from (18), which means that the HF resistance caused by variation of the current is a second-order error and can be neglected. By substituting (1) and (3) into (18), Δi_a^+ can be rewritten as:

$$\frac{2\Delta i_a^+}{(U_o - U_{err})T_s} = \frac{\cos^2\theta_a}{L_d^+} + \frac{\sin^2\theta_a}{L_q^+} \tag{20}$$

Similarly, during T_4^*–T_4, Δi_a^- denotes the variation of the phase A current, where $\Delta i_a^- = i^-$. The average output voltage is $-U_h$, and Δi_a^- can be derived as:

$$\frac{2\Delta i_a^-}{(U_o - U_{err})T_s} = -\frac{\cos^2\theta_a}{L_d^-} - \frac{\sin^2\theta_a}{L_q^-} \tag{21}$$

where L_d^- and L_q^- are the d-q axis inductances during T_4^*-T_4.

Magnetic saturation results in a slight variation of the inductance under a low-amplitude injected current. Nevertheless, the d-axis inductance gets greater when $i_d < 0$, and it gets smaller when $i_d > 0$. For simplified analyses, the average value of L_d^- and L_d^+ can be considered to be almost constant, and the q-axis inductance is analyzed similarly, which can be expressed as:

$$\begin{cases} \frac{2}{L_d} \approx \frac{1}{L_d^+} + \frac{1}{L_d^-} \\ \frac{2}{L_q} \approx \frac{1}{L_q^+} + \frac{1}{L_q^-} \end{cases} \tag{22}$$

From (18) to (22), in order to reduce the influence of magnetic saturation on the inductances and to eliminate the DC component of the HF current, K_a is defined as:

$$K_a = 2\frac{\Delta i_a^+ - \Delta i_a^-}{(U_o - U_{err})T_s} = \frac{2\cos^2\theta_a}{L_d} + \frac{2\sin^2\theta_a}{L_q} \tag{23}$$

Correspondingly, when the directions of the HF voltage signal injection are 'b' or 'c', as shown in Fig. 2, K_b and K_c are defined as:

$$\begin{cases} K_b = 2\frac{\Delta i_b^+ - \Delta i_b^-}{(U_o - U_{err})T_s} = \frac{2\cos^2\theta_b}{L_d} + \frac{2\sin^2\theta_b}{L_q} \\ K_c = 2\frac{\Delta i_c^+ - \Delta i_c^-}{(U_o - U_{err})T_s} = \frac{2\cos^2\theta_c}{L_d} + \frac{2\sin^2\theta_c}{L_q} \end{cases} \tag{24}$$

where Δi_b^+ and Δi_b^- are variations of the phase B currents corresponding to the average output voltages U_h and $-U_h$, when the direction of the HF voltage signal injection is 'b'. In addition, Δi_c^+ and Δi_c^- are variations of the phase C currents corresponding to the average output voltages U_h and $-U_h$, when the direction of the HF voltage signal injection is 'c'.

The estimated initial rotor position is defined as θ_a. From Fig. 2, θ_b and θ_c can be expressed as:

$$\begin{cases} \theta_b = \theta_a - \frac{2}{3}\pi \\ \theta_c = \theta_a - \frac{4}{3}\pi \end{cases} \tag{25}$$

According to (23) through (25), the solutions of the equations are:

$$\begin{cases} M_1 = \frac{1}{3}(K_a + K_b + K_c) = \frac{1}{L_d} + \frac{1}{L_q} \\ M_2 = \frac{\sqrt{3}}{3}(K_c - K_b) = (\frac{1}{L_d} - \frac{1}{L_q}) \sin 2\theta_a \\ M_3 = \frac{1}{3}(2K_a - K_b - K_c) = (\frac{1}{L_d} - \frac{1}{L_q}) \cos 2\theta_a \end{cases} \tag{26}$$

Here, L_d, L_q, and θ_a can be obtained as:

$$\begin{cases} L_d = \dfrac{2}{M_1 + \sqrt{M_2^2 + M_3^2}} \\ L_q = \dfrac{2}{M_1 - \sqrt{M_2^2 + M_3^2}} \\ \theta_a = \dfrac{1}{2} \arctan \dfrac{M_2}{M_3} \end{cases} \tag{27}$$

Twice the estimated rotor angle in (26) leads to ambiguity of the magnetic polarity, which means that the position estimation error can be either 0 or π. To clear up this ambiguity, magnetic polarity identification utilizing a short pulse is applied and introduced in Sect. 4.

From (20) and (21), there is a linear relationship between the output voltage amplitude U_o and the current variation Δi. To further reduce the estimation error, the least square method is applied to fitting U_o and Δi. Therefore, $\Delta {i_a}^+$, $\Delta {i_a}^-$, and K_a can be rewritten as:

$$\begin{cases} \Delta i_a^+ = k_a^+ U_o + b_a^+ \\ \Delta i_a^- = k_a^- U_o + b_a^- \\ K_a = 2\frac{k_a^+ - k_a^-}{T_s} \end{cases} \tag{28}$$

where ${k_a}^+$ and ${k_a}^-$ are the slopes of the fitting lines, and ${b_a}^+$ and ${b_a}^-$ are the intercepts of the fitting lines. K_b and K_c are similar to K_a. It is worth mentioning that U_{err} is absent from (28), which means U_{err} has no impact on the estimation accuracy when using the least square method. Thus, an accurate value of U_{err} is unnecessary. An overall control block diagram of the parameter estimation method is shown in Fig. 10.

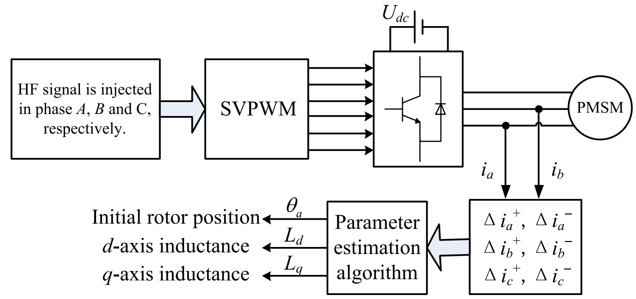

Fig. 10 Control block diagram of the parameter estimation method

4 Experimental results

Figure 11 shows a PMSM driven experimental platform, where the main parameters are shown in Table 3. A PS21865 intelligent power module (IPM) is used for the VSI, and a TMS320F28335 digital signal processor (DSP) is used for the controller.

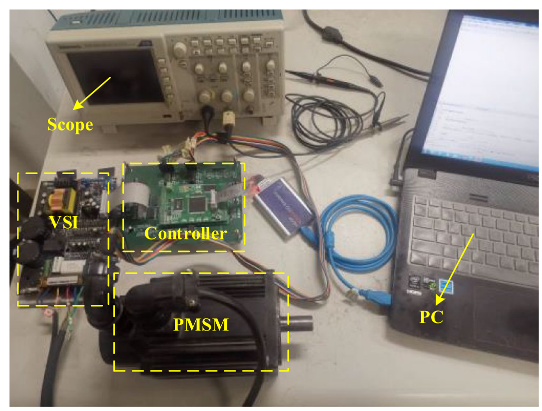

Fig. 11 PMSM driven experimental platform

Table 3 PMSM driven experimental system parameters

Parameter	Symbol	Value
Pole pairs	p	4
Rated speed	n	3000 r/min
Rated current	I_N	4.2A
Rated power	P_N	1 kW
Winding resistance	R_s	0.5 Ω
d-axis inductance	L_d	1.33 mH
q-axis inductance	L_q	1.65 mH
DC bus voltage	U_{dc}	311 V
Switching frequency	f_{sw}	10 kHz
Sampling frequency	f_{sample}	10 kHz
Dead time	T_d	4 μs

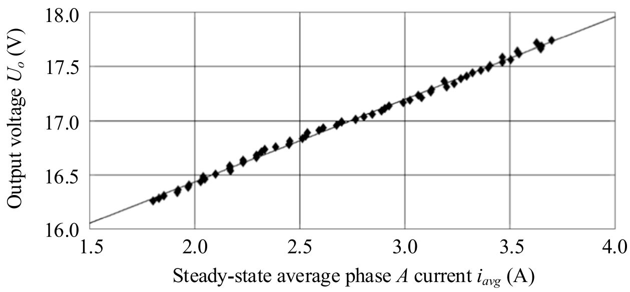

Fig. 12 Data of U_o and i_{avg} and their fitting line

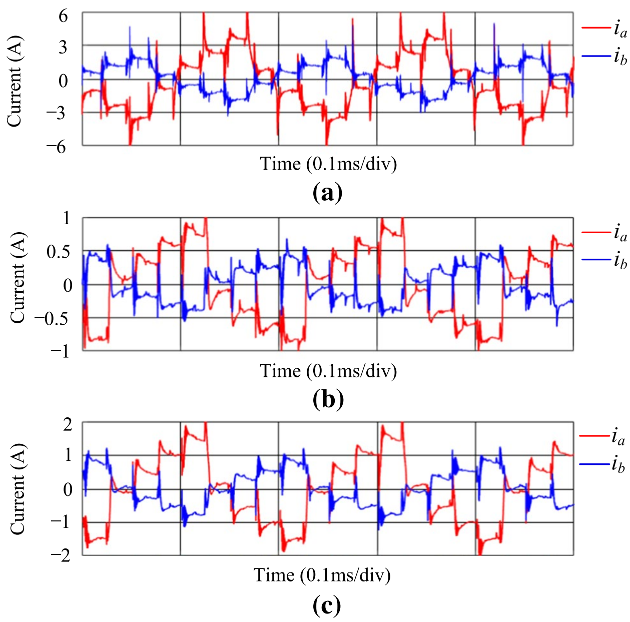

Fig. 13 Phase A and phase B current waveforms under different HF voltages: **a** $U_o=50$ V; **b** $U_o=19$ V; **c** $U_o=28$ V

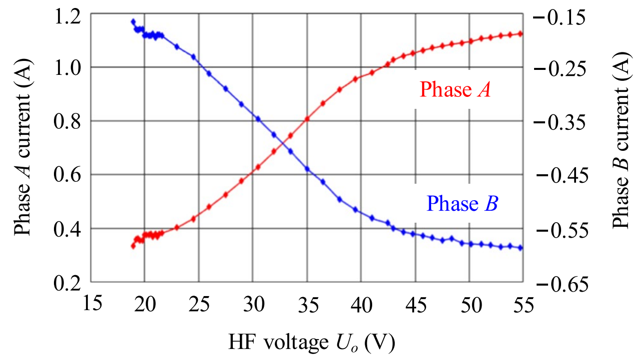

Fig. 14 Phase A and phase B current values after the currents cross the zero level

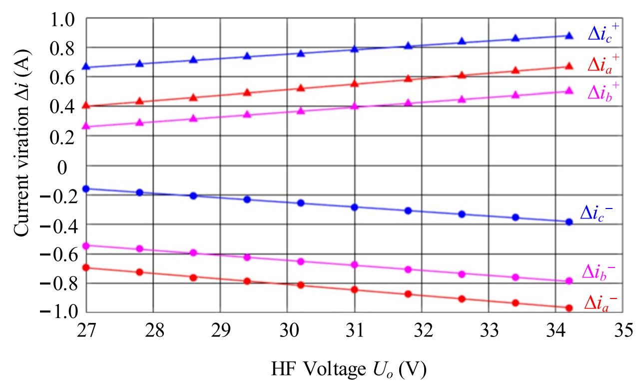

Fig. 15 Relationship between the HF voltage amplitude U_o and the current variation Δi along with their fitting lines

The DC bus voltage U_{dc}, the phase A current i_a, and the phase B current i_b are sampled at the beginning moment of each switching period. The phase C current i_c is equal to $-(i_a+i_b)$ due to the Y-connected windings of the PMSM. According to (7), Fig. 12 shows the data of U_o and i_{avg} and their fitting line $U_o=0.76R_s+15$. From experimental results, R_s is 0.51 Ω and U_{err} is 15 V. According to (3), U_{err} should be 16.6 V. This error is due to the fact that the other factors that led to inverter nonlinearity are neglected in (3). Nevertheless, the error is not significant which means the dead-time is the main factor causing inverter nonlinearity.

When the direction of the HF voltage signal injection is 'a', Fig. 13 shows the phase A and B steady-state currents under different HF voltages. Figure 13a depicts the currents corresponding to Fig. 4 when r is greater than 2.5 and U_o is set to 50 V. Figure 13b shows the currents corresponding to Fig. 7 when the range of r is 1.25–1.5 and U_o is set to 19 V. Figure 13c shows the currents corresponding to Fig. 8 when the range of r is 1.5–2.5 and U_o is set to 28 V. As can be seen from Fig. 13, there are different phenomena corresponding to the different r ranges when the currents cross the zero level. It is evident that currents clamp to the zero level in Fig. 13c.

Figure 14 illustrates the relationship between the HF voltage amplitude U_o and the phase A current i^+ in Table 2. There are 14 sampling points in the different r ranges. The corresponding phase B current also is shown in Fig. 14. When U_o is 19–22.5 V (r is 1.25–1.5), the currents are almost constant. When U_o is 22.5–37.5 V (r is 1.5–2.5), the currents increase linearly with U_o. When U_o is greater than 37.5 V (r is greater than 2.5), the currents slowly increase due to the inductance decrease caused by magnetic saturation.

From Fig. 14, the range of the HF voltage amplitude should be set to 27–35 V to utilize the ZCC effect and to obtain the linear relationship. Figure 15 illustrates the HF voltage amplitude U_o and the current variations Δi along with their least square method-based fitting lines under different directions of signal injection. The slopes of these fitting lines can be used for parameter estimation to improve

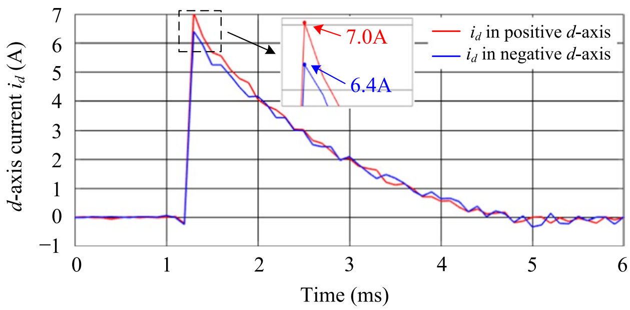

Fig. 16 *d*-axis currents of the magnetic polarity identification

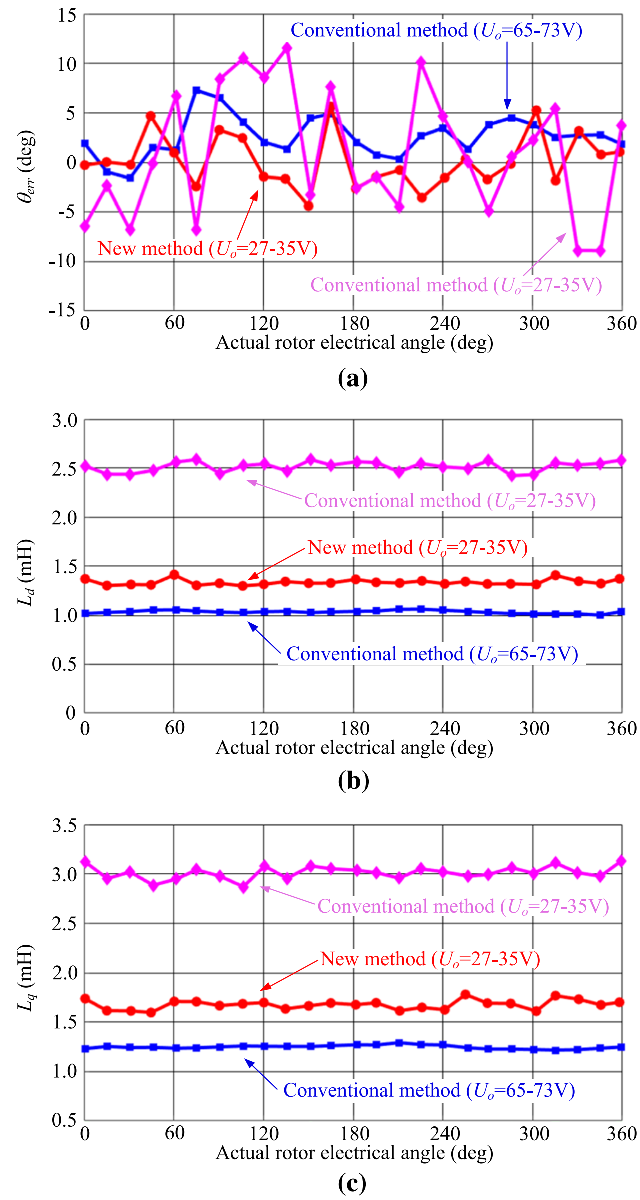

Fig. 17 Estimation results of the conventional method and the proposed method: **a** rotor position estimation error; **b** estimation value of the *d*-axis inductance; **c** estimation value of the *q*-axis inductance

accuracy. The duration of the injected HF signal is 50 ms. For the first 20 ms, the steady-state is achieved and then 150 data points of Δi^+ and Δi^- are sampled for the rest of the time. The values of Δi^+ and Δi^- in Fig. 15 are the average values of these 150 data points.

From (27), θ_a is the estimated rotor position, and the method of magnetic polarity identification is given as follows. When three-phase currents are zero, the inverter outputs a high-amplitude voltage vector in the θ_a direction in a switching period. At the end of the switching period, the *d*-axis current is sampled. Similarly, the inverter outputs a voltage vector with the same amplitude in the $\theta_a + \pi$ direction, and the *d*-axis current is likewise sampled at the end of the switching period. Figure 16 shows the *d*-axis currents when the short voltage pulse amplitude is 105 V. For ease of comparison, two periods of generating voltage pulses are overlapped. The *d*-axis current in the positive *d*-axis is greater than the other one.

The initial rotor position and the *d*-*q* axis inductances are estimated using the least square method according to (28). The HF voltage amplitude is the same as the voltage amplitude in Fig. 15. In the conventional method, the output voltage variation caused by the dead-time effect is considered to be constant, and its amplitude is equal to U_{err}. According to the analysis in this paper, its amplitude relates to the amplitude of the output voltage. The rotor position estimation error θ_{err} and the estimated *d*-*q* axis inductances L_d and L_q are depicted in Fig. 17. There are two experimental results for the conventional methods in Fig. 17. The first is to use the same HF injected signal as the new method, the second is to use a high amplitude HF injected signal. In the experiment with high amplitude HF signal injection, the rotor is fixed to remain stationary. From Fig. 17, under low amplitude HF excitation, the estimation error of the conventional method is greater than the new method since the voltage variation caused by the dead-time effect is incorrect. By increasing the amplitude of the output voltage, the dead-time effect can be mitigated. However, high amplitude current can cause the rotor to rotate. Thus, the rotor has to be fixed. Moreover, high amplitude current can cause serious magnetic saturation. Thus, the estimation values of the inductances are smaller than the actual values.

The experimental results of the new method are shown in detail in Fig. 18. The average error of θ_{err} is 2.0 °. The maximum error of θ_{err} is 5.6 °. The average estimations of L_d and L_q are 1.33mH and 1.68mH, respectively. Their maximum relative errors are 6.1% and 7.9%. In addition, the average values are 1.6% and 2.8%. It can be seen from these experimental results that the proposed method can estimate the rotor position and the *d*-*q* axis inductances.

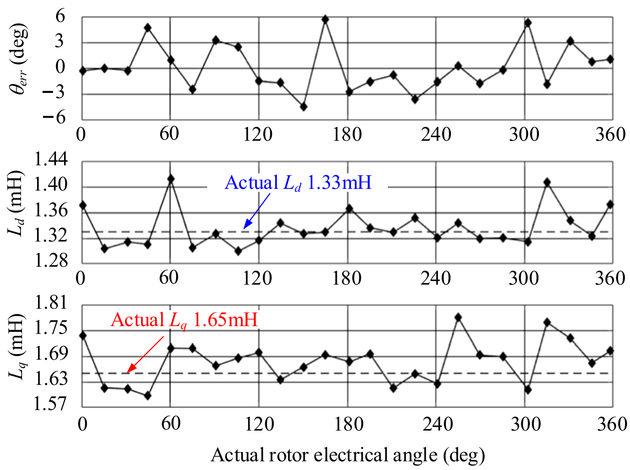

Fig. 18 Error of the rotor position estimation and the estimated *d*-*q* axis inductances with the least square method

5 Conclusion

In this paper, a method for initial rotor position and inductance estimations is proposed for the sensorless control of a PMSM by utilizing the ZCC effect. To simplify the analysis of the dead-time effect, a HF signal must be injected in the three-phase stationary reference frame and its period must be four times the switching period. The amplitude of the HF signal is only 1.5–2.5 times the voltage variation caused by the dead-time effect, which means the dead-time can cause severe distortion of the HF signal. Thus, the conventional method is unable to estimate the initial rotor position and inductances. The voltage variation caused by the dead-time effect is related to the power switches and the DC bus voltage. Generally, the dead-time of the power switches in a definite inverter is constant. Reducing the DC bus voltage means that maximum speed of the PMSM is reduced. However, in order to keep the rotor stationary, the injected HF signal should be a low amplitude and a severe dead-time effect cannot be avoided. The method proposed in this paper can solve this problem easily and without complexity in the signal demodulation process or observer design. It is worth mentioning that an accurate assessment of the voltage variation caused by the dead-time effect is unnecessary in this method. It is only used for determining the range of the HF voltage signal that can cause the ZCC effect. Thus, the proposed method is effective under different dead-time conditions. A longer dead-time means that the parameter estimation data can be sampled in a wider range of HF voltage signals, which is beneficial for improving the estimation accuracy. If the dead-time is short, the conventional method is simple and effective.

Acknowledgements This work was supported in part by the National Natural Science Foundation of China under Grant 51607091.

References

1. Zhu, Z.Q., Liang, D., Liu, K.: Online parameter estimation for permanent magnet synchronous machines: an overview. IEEE Access. **9**, 59059–59084 (2021)
2. Liu, X., Chen, H., Zhao, J., Belahcen, A.: Research on the performances and parameters of interior PMSM used for electric vehicles. IEEE Trans. Ind. Electron. **63**(6), 3533–3545 (2016)
3. Degner, M.W., Lorenz, R.D.: Using multiple saliencies for the estimation of flux, position, and velocity in AC machines. IEEE Trans. Ind. Appl. **34**(5), 1097–1104 (1998)
4. Jang, J.-H., Sul, S.-K., Ha, J.I., Ide, K., Sawamure, M.: Sensorless drive of surface-mounted permanent-magnet motor by high-frequency signal injection based on magnetic saliency. IEEE Trans. Ind. Appl. **39**(4), 1031–1039 (2003)
5. Yoon, S.-C., Kim, J.-M.: Sensorless control of a PMSM at low speeds using high frequency voltage injection. J. Power Electron. **5**(1), 11–19 (2005)
6. Shuang, B., Zhu, Z.-Q.: A novel sensorless initial position estimation and startup method. IEEE Trans. Ind. Electron. **68**(4), 2964–2975 (2021)
7. Kim, S., Im, J., Song, E., Kim, R.: A new rotor position estimation method of IPMSM using all-pass filter on high-frequency rotating voltage signal injection. IEEE Trans. Ind. Electron. **63**(10), 6499–6509 (2016)
8. Bi, G., Wang, G., Zhang, G., Zhao, N., Xu, D.: Low-noise initial position detection method for sensorless permanent magnet synchronous motor drives. IEEE Trans. Power Electron. **35**(12), 13333–13344 (2020)
9. Li, H., Zhang, X., Yang, S., Liu, S.: Unified graphical model of high-frequency signal injection methods for PMSM sensorless control. IEEE Trans. Ind. Electron. **67**(6), 4411–4421 (2020)
10. Wang, G., et al.: Self-commissioning of permanent magnet synchronous machine drives at standstill considering inverter nonlinearities. IEEE Trans. Power Electron. **29**(12), 6615–6627 (2014)
11. Ben-Brahim, L.: On the compensation of dead time and zero-current crossing for a PWM-inverter-controlled AC servo drive. IEEE Trans. Ind. Electron. **51**(5), 1113–1117 (2004)
12. Liu, K., Zhu, Z.Q., Zhang, Q., Zhang, J.: Influence of nonideal voltage measurement on parameter estimation in permanent-magnet synchronous machines. IEEE Trans. Ind. Electron. **59**(6), 2438–2447 (2012)
13. Wang, G., Wang, Y., Ding, L., Yang, L., Ni, R., Xu, D.: Harmonic analysis of the effects of inverter nonlinearity on the offline inductance identification of pmsms using high frequency signal injection. J. Power Electron. **15**(6), 1567–1576 (2015)
14. Qiu, T., Wen, X., Zhao, F.: Adaptive-linear-neuron-based dead-time effects compensation scheme for PMSM drives. IEEE Trans. Power Electron. **31**(3), 2530–2538 (2016)
15. Kim, S., Lee, W., Rho, M., Park, S.: Effective dead-time compensation using a simple vectorial disturbance estimator in PMSM drives. IEEE Trans. Ind. Electron. **57**(5), 1609–1614 (2010)

16. Park, Y., Sul, S.-K.: A novel method utilizing trapezoidal voltage to compensate for inverter nonlinearity. IEEE Trans. Power Electron. **27**(12), 4837–4846 (2012)

Jing Wang received his B.S. degree in Electrical Engineering from the Nanjing University of Science and Technology, Nanjing, China, in 2019, where he is presently working towards his M.S. degree in Electrical Engineering. His current research interests include the control of permanent magnet synchronous motors.

Jianhu Yan received his B.S. degree in Electrical Engineering from the Nanjing University of Science and Technology, Nanjing, China, in 2005; and his Ph.D. degree in Electrical Engineering from Southeast University, Nanjing, China, in 2013. In 2013, he became an Assistant Professor in the School of Automation, Nanjing University of Science and Technology, where he has been working as an Associate Professor since 2018. His current research interests include the design and control of permanent magnet machines.

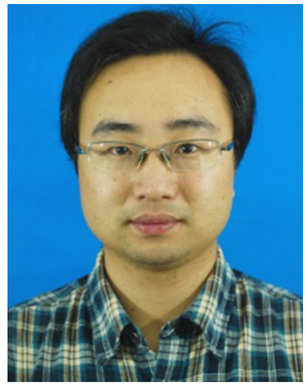

Zhanfeng Ying received his B.S. degree in Control Science and Engineering from the Shenyang Aerospace University, Shenyang, China, in 2004; and his Ph.D. degree in Engineering Mechanics from the Nanjing University of Science and Technology, Nanjing, China, in 2009. He is presently working as an Associate Professor in the School of Energy and Power Engineering, Nanjing University of Science and Technology. His current research interests include the reliability assessment of power electronic devices.